

Eightfold quasipatterns in an optical pattern-forming system

A. Aumann,^{*} T. Ackemann,[†] E. Große Westhoff,[‡] and W. Lange[§]

*Institut für Angewandte Physik, Westfälische Wilhelms-Universität Münster, Corrensstr. 2/4, D-48149 Münster,
Federal Republic of Germany^{||}*

(Received 4 April 2002; published 28 October 2002)

Quasipatterns with an eightfold rotational symmetry and irregular two- and three-mode patterns are found in an experiment on optical pattern formation. The patterns exist in the transverse cross section of a laser beam that traverses a system built from a sodium vapor cell and a plane feedback mirror with a quarter-wave plate placed into the feedback loop. The occurrence of the quasipatterns is reproduced by numerical simulations and explained by amplitude equations that contain only odd-order terms and are derived from the microscopic model. The selection process is governed by the angle dependence of the cubic cross coupling coefficients in the amplitude equations. Up to our knowledge it provides the first experimental example for a stabilization mechanism proposed earlier that is based on an oscillatory dependence of the cubic cross coupling coefficient on the angle between the interacting wave vectors. The relationship to the prediction of quasipatterns in a similar setup without additional wave plate [Phys. Rev. A **53**, 1072 (1996)] is discussed.

DOI: 10.1103/PhysRevE.66.046220

PACS number(s): 89.75.Kd, 42.65.Sf, 47.54.+r, 42.25.Ja

I. INTRODUCTION

States that are quasiperiodic in space are known to occur in equilibrium systems [quasicrystals [1,2]], as well as in self-organizing dissipative systems driven far from equilibrium [3–7]. Quasiperiodic states represent a remarkable phase that has no periodicity in spite of a Fourier spectrum with well defined peaks and a well defined rotational symmetry [see e.g., Ref. [1] and references therein]. Two-dimensional realizations of quasiperiodic spatial states in dissipative systems are often called *quasipatterns*. Their properties and stabilization mechanisms have been a matter of considerable interest [e.g., Refs. [8–13]]. Quasipatterns with a twelvefold rotational symmetry were experimentally observed [4,7] in systems without inversion symmetry. This particular configuration of a quasipattern is expected in these systems since it is favored by quadratic coupling terms [8,9,11,14,15].

In systems with inversion symmetry the amplitude equations describing the dynamics of the bifurcating modes close to threshold contain only odd-order terms [16]. In this case it was shown that different kinds of quasipatterns with eightfold, tenfold, twelvefold, or fourteenfold rotational symmetries might be stable. The selection of a particular symmetry is determined by the dependence of the cubic cross coupling coefficient on the angle between the interacting wave vectors [8–10,12,13,17]. In a Faraday experiment [3,6] quasipatterns with an eightfold and tenfold rotational symmetries were observed indeed, in good agreement with theoretical predictions [12,13]. Furthermore it was predicted that in principle one can “engineer” quasipatterns of arbitrary rotational symmetry by adding suitable terms involving high-order spatial

derivatives to the model equations [9,17]. On the level of the amplitude equations these derivatives manifest themselves in an oscillatory dependence of the cubic cross coupling coefficient on the angle between the interacting wave vectors. We are not aware of a report in the literature on an experimental observation of a quasipattern relying on an oscillatory cross-coupling coefficient. As noted in Ref. [10] optical pattern forming systems might be very well suited to demonstrate this phenomenon since the diffraction occurring for propagation over a finite distance leads naturally to the occurrence of higher order derivatives. Thus we will address experimentally and theoretically the formation of quasipatterns in a nonlinear optical system in this paper.

The experimental system [see Fig. 1] is built from a nonlinear medium and a single mirror [18–21]. The medium is irradiated by an enlarged and collimated laser beam. During the propagation to the mirror and back different points in the transverse cross section of the beam are coupled by diffraction. If sodium vapor is used as the nonlinear medium, the spontaneous emergence of squares in the transverse beam profile is observed for linear input polarization and a positive detuning between the frequency of the laser beam and the sodium D_1 resonance line [22]. This is in accordance with theoretical expectation [10,22–26]. For negative detuning experimentally no pattern formation was observed [22], although eightfold quasipatterns were predicted to occur in a

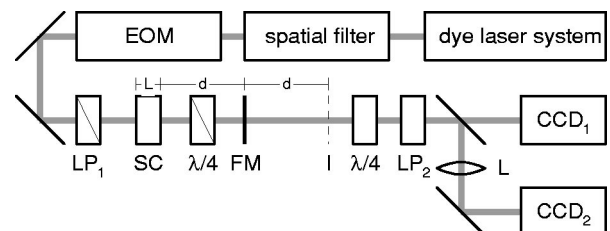


FIG. 1. Schematic of the experimental setup. EOM: electro-optic modulator; $LP_{1/2}$: linear polarizers; SC: sodium cell; $\lambda/4$: quarter-wave plate; FM: feedback mirror; L: focusing lens; CCD_1 , CCD_2 : charge coupled device cameras. See, text for details.

^{*}Andreas. Aumann@gmx.de

[†]t.ackemann@uni-muenster.de

[‡]grosse.westhoff@uni-muenster.de

[§]w.lange@uni-muenster.de

^{||}<http://www.uni-muenster.de/Physik/AP/Lange/Welcome-e.html>

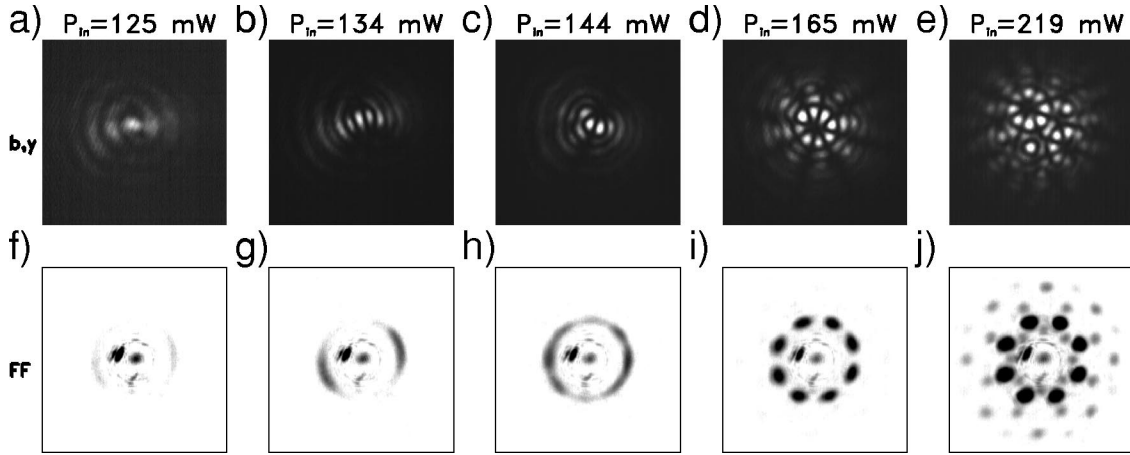


FIG. 2. Patterns obtained for increasing input power. The images (a)–(e) show the intensity distribution of the backward beam viewed through a polarization analyzer, as explained in the text. The images (f)–(j) show the optical Fourier transform of the transmitted beam. Parameters: $T=341\text{ }^{\circ}\text{C}$, $\Delta=8\text{ GHz}$, $d=210\text{ mm}$, $p_{N_2}=300\text{ hPa}$. The images—and all following ones—are depicted in a linear gray level scale. In the near field images “white” denotes high intensity, whereas in the far field images “black” denotes high intensity. The frame size of the near field images corresponds to $4\times 4\text{ mm}^2$ (integration time 1 ms). The frame size of the far field images corresponds to $60\times 60\text{ mm}^2$. The far field images show a small intense spot at the 10 o’clock position within the ring belonging to the critical wave number. This spot is due to a parasitic reflection in the imaging system and is not related to pattern formation.

limiting case [no absorption, no diffusion [10,27]]. In the same limit the introduction of a quarter-wave plate in the feedback loop is equivalent to an exchange of the sign of the detuning [25]. It turns out that under the conditions of the real experiment the introduction of the quarter-wave plate favors spatial instabilities [28] and a pattern forming instability can be found on both sides of the sodium D_1 line in this configuration [29]. For a negative frequency detuning from the resonance, square patterns are found [29], which are similar to those observed for a positive detuning in the system without a quarter-wave plate in the feedback loop [22]. For positive detuning, a new phenomenology arises which is described and analyzed in this paper.

II. EXPERIMENT

A. Experimental setup

A schematic of the experimental setup is shown in Fig. 1. The output of a cw dye laser, operating within a range of some atomic linewidths above the D_1 resonance, is being spatially filtered using a single-mode fiber and expanded to a $1/e^2$ radius of 1.5 mm. The residual geometrical ellipticity of the beam is lower than 1%. An electro-optic modulator is used for stabilization or scanning of the input power. Finally, a linear polarizer (LP_1) ensures a linear polarization of the laser beam.

This laser beam is injected into a heated cell (length $L=15\text{ mm}$) containing sodium vapor in a buffer gas atmosphere of 300 hPa N_2 . The buffer gas provides a strong homogeneous broadening, which masks both the hyperfine splitting and the Doppler broadening of the sodium D_1 line, and quenches efficiently the occupation of the excited state. A cell temperature of about $340\text{ }^{\circ}\text{C}$ results in a sodium particle density of $\approx 10^{14}\text{ cm}^{-3}$. Two pairs of Helmholtz coils are used for compensation of static magnetic field compo-

nents transverse to the propagation axis of the laser beam to less than $1\text{ }\mu\text{T}$. A longitudinal magnetic field component of $B_z\approx 200\text{ }\mu\text{T}$ is applied to define the axis of quantization and to reduce the effect of residual stray fields. A plane mirror with a reflection coefficient of $R=0.99$ is positioned at a distance d of typically 200–300 mm behind the center of the cell.

In the light transmitted by the mirror, a second quarter-wave plate undoes the change of polarization due to the wave plate between the sodium cell and the feedback mirror. A linear polarizer (LP_2) is adjusted such that only the linear polarization component orthogonal to the input polarization is transmitted. Thus the appearance of a signal behind this polarizer indicates a polarization instability [see also Ref. [21]]. Patterned states appear also in the total transmitted power as well as in the polarization component parallel to the input polarization but the observation is done in the orthogonal one since this component displays a pattern on zero background, i.e., the contrast is optimum. A charge coupled device (CCD) camera records the intensity distribution in the transverse plane positioned at a distance d behind the mirror. In this plane the field distribution corresponds to the one of the reflected beam at the position of the cell. In the following, we will refer to this intensity distribution as the “near field picture” of the backward beam. A second CCD camera records the Fourier spectrum of the light field, which is obtained in the focal plane of a lens. We will refer to it as the “far field picture.”

B. Experimental results: Patterns

Figure 2 shows a typical sequence of patterns observed in a scan of the input power. The upper row displays the near field patterns, the lower row the corresponding far field patterns; the input power increases from left to right.

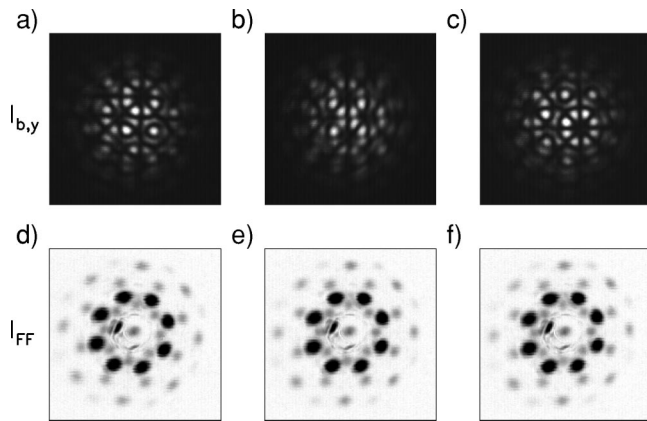


FIG. 3. Eightfold quasipatterns. The upper row of images (a)–(c) shows the intensity distribution of the backward beam (integration time 1 ms). The lower row of images (d)–(f) shows the optical Fourier transform of the transmitted beam. Parameters as in Fig. 2(e).

At a power threshold of $P_{in} = 125$ mW a weak signal consisting of a bright spot surrounded by three fragmented rings appears in the near field, see Fig. 2(a). In the optical Fourier transform, shown in Fig. 2(f), there are two ring fragments lying opposite to each other. The bifurcation is supercritical within the accuracy of the experiment. For an input power of $P_{in} = 134$ mW, the modulation of the near field intensity profile is more pronounced and consists of a number of oval spots and ring fragments, see Fig. 2(b). The optical Fourier transform displays two ring fragments [Fig. 2(g)]. At an input power level of $P_{in} = 144$ mW, a modulated ring system surrounds two bright spots in the center of the laser beam, see Fig. 2(c). The optical Fourier transform, shown in Fig. 2(h), consists of a bright ring indicating the emergence of a characteristic spatial wave number. Superimposed on this ring, eight local maxima can be seen. Fig. 2(d) shows a pattern on the backward beam for an input power of $P_{in} = 165$ mW. Close to the center of the laser beam, eight bright spots are observed. The pattern has an approximate eightfold rotational symmetry. The corresponding optical Fourier transform is composed of eight bright spots which are regularly distributed on a circle. Finally, for the highest available input power of $P_{in} = 219$ mW, a complex pattern is observed which does not show any apparent translational or rotational symmetry, see Fig. 2(e). The corresponding optical Fourier transform is composed of five systems of eight bright spots regularly distributed on circles corresponding to different wave numbers, see Fig. 2(j). The lesser intense spots can be interpreted as harmonics of the most intense fundamental modes. Three sets of harmonics have a higher wave number than the fundamental modes and result from mixing of one mode with itself, with its next neighbor, or with its second next neighbor. One set of harmonics has a lower wave number than the fundamental modes and results from mixing between two fundamental wave vectors enclosing a mutual angle of 135° .

For nominally constant parameters different patterns are found in the near field of the backward beam in consecutively acquired images, see Figs. 3(a)–3(c). The consecu-

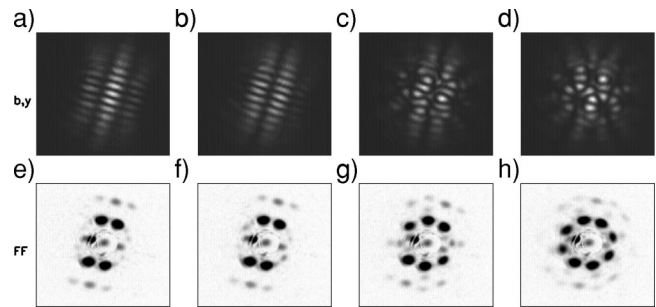


FIG. 4. Two- and three-mode patterns. The images (a)–(d) show the intensity distribution of the backward beam viewed through a polarization analyzer, as explained in the text (integration time 0.25 ms). The images (e)–(h) show the optical Fourier transform of the transmitted beam. Parameters: $P_{in} = 200$ mW, $T = 340^\circ\text{C}$, $\Delta = 6$ GHz, $d = 266$ mm, $p_{N_2} = 300$ hPa.

tively acquired images of the optical Fourier transform of the transmitted beam, shown in Figs. 3(d)–3(h), are almost identical. They are composed of four pairs of fundamental modes mutually at an angle of $45^\circ \pm 2^\circ$, plus several sets of spatial harmonics. In contrast, the near field patterns might change completely from one half frame of the video camera system to the next one, i.e., within 20 ms. On the other hand, there are no indications of a change of the near field patterns within the integration time of a snapshot which was 1 ms. The time scale of alternation between the different near field patterns is typically some tens of milliseconds. These observations indicate that the observed patterns are metastable states which are linked by transition phases of rather short duration. The experiments performed do not allow to identify the nature of the transition process.

The near field patterns do not possess any apparent translational symmetry. However, all these patterns contain characteristic substructures of eight intensity maxima on a circle. In the individual pictures, the relative positions of these substructures differ, but the orientation of these substructures with respect to each other is fixed. This means, there is a *long range* orientational order which characterizes these patterns. The far field patterns have an approximate eightfold rotational symmetry, which is known to be incompatible with a translational symmetry of the corresponding near field images [e.g., Ref. [8]].

We interpret these structures as small portions of a spatially extended quasipattern. The observed alternation between different near field patterns is apparently due to noise-driven switching between different—approximately equally likely—realizations of this ‘ideal’ pattern in the limited beam. A similar behavior with similar time scales was found before for hexagonal patterns with a different number of constituents or different orientation [20,30]. Far above threshold, the quasipatterns are the predominant structures. Once they are formed, they persist when the input power is increased, i.e., no secondary bifurcations from eightfold quasipatterns to other structures have been observed.

Aside from eightfold quasipatterns, patterns with an optical Fourier transform composed of two and three pairs of modes are found. Examples are given in Fig. 4. Rhombic patterns composed of a regularly ordered set of oval intensity

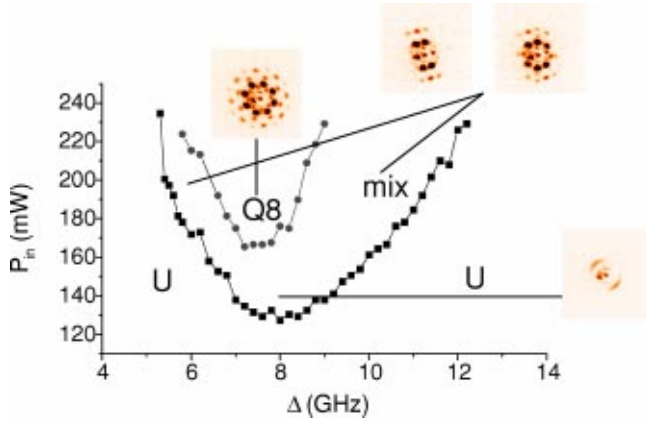


FIG. 5. (Color online) Stability diagram of patterns obtained for different values of the input power P_{in} and detuning Δ . See text. Parameters: $T = 340^\circ\text{C}$, $d = 210$ mm, $p_{N_2} = 300$ hPa.

maxima, see Figs. 4(a) and 4(b), are dominant for the set of parameters chosen in Fig. 4. The optical Fourier transform of these patterns is composed of four intensity maxima corresponding to two principal Fourier modes of equal wave number, see Figs. 4(e) and 4(f). These two principal modes are at an angle of $40^\circ \pm 1^\circ$. Three more sets of Fourier modes can be observed, which can be interpreted as spatial harmonics of the principal modes.

For nominally identical parameters—in coexistence with the two-mode patterns—patterns with an optical Fourier transform composed of three principal modes or of four pairs of Fourier peaks at the same wave number but of unequal intensity can be observed. An example for a three-mode pattern is shown in Fig. 4(g). Two of the three modes, which are at an angle of $41^\circ \pm 1^\circ$, are equally intense; a third mode is weaker and forms an angle of $46^\circ \pm 1^\circ$ with one of the more intense modes. The corresponding near field intensity distribution is composed of rather irregularly distributed intensity maxima [Fig. 4(c)]. In Fig. 4(h) an example for a four-mode pattern is displayed. The angle between the most intense modes is $42^\circ \pm 1^\circ$, the angle between the less intense modes is $48^\circ \pm 1^\circ$. The corresponding images of the near field resemble the near field images of the eightfold quasipatterns discussed above.

C. Experimental results: Stability diagram

The behavior of the system in dependence on the two parameters input power and frequency detuning is summarized in the stability diagram shown in Fig. 5. For low input power, the Gaussian input beam is homogeneously absorbed. There is no emission of light in the linear polarization component orthogonal to the input polarization. This state of the system is denoted by U in Fig. 5.

The black squares indicate the minimum input power levels at which an instability of the beam profile is observed. The power threshold of the pattern forming instability has a local minimum at a frequency detuning of 8 GHz. For frequency detunings smaller than 5 GHz and larger than 13 GHz the power threshold exceeds the available input power. Directly above the power threshold of the instability, far field

patterns composed of fragmented rings are observed. The corresponding near field patterns are similar to those shown in Figs. 2(a) and 2(b).

An increase of the input power leads to the formation of patterns, which possess an optical Fourier transform composed of a clearly defined set of principal modes. There exists a region in the parameter space, in which exclusively eightfold quasipatterns are observed. This region is denoted by Q8 in the diagram.

In those parts of the instability region which are disjoint with the region denoted by Q8, nonstationary two- and three-mode structures can be found. At low input power they coexist typically with the fragmented ring structures, which are observed directly at threshold. At high input power levels, as indicated in the diagram, the two- and three-mode patterns become dominant, but coexist with four-mode patterns. However, it is not possible to specify a closed region of stability of the two- or three-mode patterns. This region of coexistence of different patterns is denoted by mix in the diagram.

The structure of the parameter space displayed in Fig. 5 is characteristic for the system under consideration. The structure is found to be qualitatively independent of the sodium cell temperature, which controls the particle number density of the sodium atoms. Moreover, it is found to be qualitatively independent of the distance d between the sodium cell and feedback mirror. Of course, the range of cell temperatures and the range of d for which patterns can be found, respectively, are limited by the available input power and the finite width of the Gaussian beam. The observed behavior is not affected by a rotation of the quarter-wave plate inside the feedback loop.

III. THEORY

A. The model

The microscopic description of any optical pattern forming system involves the self-consistent calculation of the nonlinear dielectric polarization [31] of the medium and of the propagation of the light field within the system.

The conditions of the present experiment have been chosen in such a way that the sodium D_1 line can be treated as a homogeneously broadened $J = \frac{1}{2} \leftrightarrow J' = \frac{1}{2}$ transition with a negligible population of the excited state [32]. In a formal description [33,34] the light matter interaction is treated in the framework of the density matrix formalism [31]. The result of this treatment is an expression for the nonlinear susceptibility χ_{\pm} of the medium for the σ_{\pm} circular polarization components of the light field. It is given by $\chi_{\pm} = \chi_{lin}(1 \mp w)$, where w denotes the so-called orientation of the vapor, i.e., the normalized population difference between the two Zeeman sublevels of the ground state of the sodium atom.

$$\chi_{lin} = - \frac{N_{Na} |\mu_e|^2}{2 \epsilon_0 \hbar \Gamma_2} \frac{\bar{\Delta} + i}{\bar{\Delta}^2 + 1} \quad (1)$$

denotes the linear susceptibility of the medium. N_{Na} is the particle number density of the sodium atoms, $\mu_e = 1.72$

$\times 10^{-29}$ Cm is the dipole matrix element of the transition. $\bar{\Delta} = 2\pi\Delta/\Gamma_2$ is the detuning $\Delta = \nu_{\text{laser}} - \nu_{D_1}$ of the laser beam with respect to the sodium D_1 -line normalized to the so-called transverse relaxation rate Γ_2 , i.e., the relaxation rate of the dipole moment of the transition.

The propagation of the light field is calculated in the paraxial approximation [31]. It is assumed that the light field is purely transverse and that no new frequency components are created by the interaction of the light field with the medium. The medium is considered to be thin, so that diffraction can be neglected during the propagation of the light field through the medium [10,19]. In the description of many single feedback mirror systems the absorption of the light field is also neglected [10,21,25]. In the present experimental situation, however, absorption is not negligible [22]. We abandon this approximation and follow a recently demonstrated refined approach [23] which employs a longitudinal average ϕ of orientation w ,

$$\phi(\vec{r}_\perp, t) = \frac{1}{L} \int_0^L w(\vec{r}_\perp, z, t) dz. \quad (2)$$

In addition, we consider the effect of atomic diffusion, which provides a wave number depending damping of structures in the orientation. The resulting equation of motion for the longitudinal average ϕ of the orientation of the vapor is

$$\begin{aligned} \frac{\partial}{\partial t} \phi(\vec{r}_\perp, t) = & -(\gamma - D\nabla_\perp^2) \phi(\vec{r}_\perp, t) + \frac{1}{2\alpha_0 L} [-P_{-,f}(\vec{r}_\perp, 0, t) \\ & + P_{-,f}(\vec{r}_\perp, L, t) - P_{-,b}(\vec{r}_\perp, L, t) + P_{-,b}(\vec{r}_\perp, 0, t) \\ & + P_{+,f}(\vec{r}_\perp, 0, t) - P_{+,f}(\vec{r}_\perp, L, t) + P_{+,b}(\vec{r}_\perp, L, t) \\ & - P_{+,b}(\vec{r}_\perp, 0, t)]. \end{aligned} \quad (3)$$

Here, the vector $\vec{r}_\perp = (x, y)^T$ denotes the transverse coordinates, $\nabla_\perp^2 = [(\partial^2/\partial x^2) + (\partial^2/\partial y^2)]$ denotes the transverse Laplacian. γ denotes the small ($\gamma \approx 1 \text{ s}^{-1}$) relaxation rate of the orientation due to collisions, D denotes the diffusion coefficient of the sodium atoms in the buffer gas atmosphere, L is the longitudinal length of the medium. $\alpha_0 = -k_0 \text{Im}(\chi_{\text{lin}})/2$ is the small signal absorption coefficient of the medium and k_0 is the vacuum wave number of the light field.

The expressions $P_{\pm,f}(\vec{r}_\perp, z, t)$ and $P_{\pm,b}(\vec{r}_\perp, z, t)$ on the right hand side of Eq. (3) are the pump rates produced by the σ_\pm circular polarization components of the forward and the backward beams, respectively. They are evaluated at the input ($z=0$) and the output ($z=L$) planes of the vapor. The pump rate is proportional to the intensity of the respective polarization component [see, the following Eqs. (4) and (8)]. Temporal delays created by the finite speed of light are neglected, since the slowest corresponding time scales ($\sim 10^{-9}$ s) are much faster than the fastest time scales in the ground state of the atomic system ($\sim 10^{-6}$ s). That is, the dynamics of the light field is adiabatically eliminated. A for-

mal integration of the paraxial wave equation yields the following expressions for the pump rates:

$$P_{\pm,f}(\vec{r}_\perp, 0, t) = \Psi |\mathcal{E}_{\pm,f}(\vec{r}_\perp, 0, t)|^2, \quad (4)$$

$$P_{\pm,f}(\vec{r}_\perp, L, t) = e^{-2\alpha_0 L(1 \mp \phi(\vec{r}_\perp, t))} P_{\pm,f}(\vec{r}_\perp, 0, t), \quad (5)$$

$$P_{\pm,b}(\vec{r}_\perp, L, t) = R \Psi |\mathbf{P} e^{i\alpha_0 L(\bar{\Delta} + i)[1 \mp \phi(\vec{r}_\perp, t)]} \mathcal{E}_{\mp,f}(\vec{r}_\perp, 0, t)|^2, \quad (6)$$

$$P_{\pm,b}(\vec{r}_\perp, 0, t) = e^{-2\alpha_0 L[1 \mp \phi(\vec{r}_\perp, t)]} P_{\pm,b}(\vec{r}_\perp, L, t), \quad (7)$$

with

$$\Psi = \frac{3}{16} \frac{|\mu_e|^2}{4\Gamma_2 \hbar^2 (\bar{\Delta}^2 + 1)}. \quad (8)$$

The propagation operator

$$\mathbf{P} = \exp \left[-i \frac{d \nabla_\perp^2}{k_0} \right] \quad (9)$$

is defined via the corresponding power series, where d is the distance between the feedback mirror and the medium. Here, $\mathcal{E}_{\pm,f}(\vec{r}_\perp, 0, t)$ denotes the slowly varying amplitude [31] of the σ_\pm circular polarization components of the forward beam at the input face of the medium. The prefactor of 3/16 in Eq. (8) is a correction factor which accounts approximately for the fact that the efficiency of optical pumping is overestimated in the $J=1/2 \rightarrow J'=1/2$ -scheme considered here compared to a complete level scheme of sodium atoms including the hyperfine structure [34]. Note that the presence of the quarter-wave plate in the feedback arm manifests itself in Eq. (6): The pump rate of the σ_- circular polarization component of the backward beam is determined by the σ_+ circular polarization component of the forward beam and vice versa.

As opposed to the simpler limiting case of a purely dispersive medium [25], a change of sign of the detuning does not transform the Eqs. (3)–(7) into those for the system without the quarter-wave plate in the feedback loop [28,29]. The fact that the dynamics of the ground state population depends only on the modulus squared of circular field components [see, Eqs. (3), (4)–(7)] and not on their phases explains, why the behavior of the system does not depend on the orientation of the principal axis of the quarter-wave plate.

Note that the longitudinally averaged orientation ϕ is the single dynamical variable describing the system. Due to the adiabatic elimination of the dynamics of the light field, all the observables of the light field can be calculated from a given transverse distribution of ϕ . In the following, we will present numerical and analytical results based on the Eqs. (3)–(7). The numerical scheme is described in Ref. [35].

B. Results of numerical simulations

Figure 6 displays the result of a numerical simulation for parameters corresponding to those of Fig. 2. A Gaussian intensity profile of the input laser beam was used and Dirichlet boundary conditions $\phi=0$ were assumed on the border of a

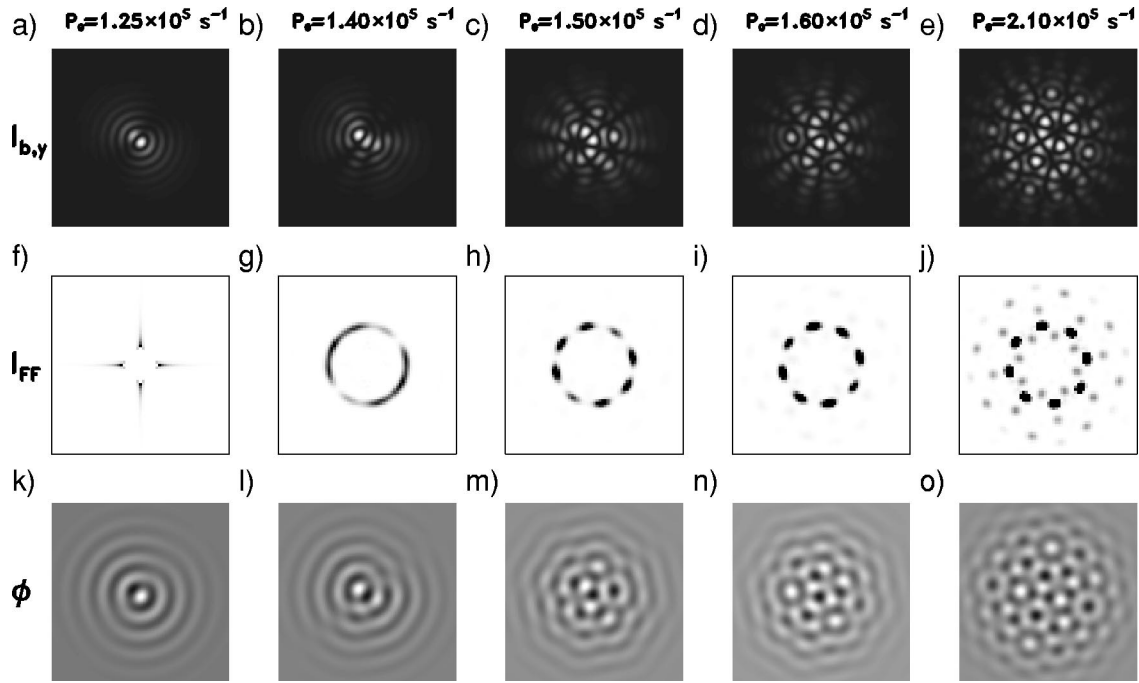


FIG. 6. Patterns for increasing pump rate P_0 of the linearly polarized Gaussian input laser beam. The images shown are the result of a numerical simulation assuming a Gaussian input laser beam and Dirichlet boundary conditions for the medium. (a)–(e) Backward near field intensity distribution of the linear polarization component orthogonal to the input polarization. (f)–(j) Total far field intensity distribution. (k)–(o) Transverse distribution of the longitudinally averaged orientation ϕ . Parameters: $N_{\text{Na}} = 1.3 \times 10^{19} \text{ m}^{-3}$, $\bar{\Delta} = 5.0$, $d = 210 \text{ mm}$, $D = 2.5 \times 10^{-4} \text{ m}^2/\text{s}$, $\Gamma_2 = 9.9 \times 10^9 \text{ s}^{-1}$. The frame size of the near field images [(a)–(e)] and of the images of the orientation [(j)–(o)] corresponds to $4 \times 4 \text{ mm}^2$. The frame size of the far field images [(f)–(i)] corresponds to $66 \times 66 \text{ mm}^{-2}$. The power of the input laser beam is in (a) 122 mW, (b) 136 mW, (c) 146 mW, (d) 156 mW, (e) 204 mW. It is calculated using that $P_{\text{in}} = c \epsilon_0 / (\pi w_0^2) (|\mathcal{E}_{+,y}(0)|^2 + |\mathcal{E}_{-,y}(0)|^2)$ and Eqs. (4), (8).

circular area with a diameter of 6 mm (for reasons of efficiency of the numerical calculations the total extent of the area represented by the numerical grid was assumed to be somehow smaller than the cell diameter of 8 mm used in the experiments; the beam radius at the $1/e^2$ -point of intensity was 1.5 mm as in the experiment). The input laser beam is linearly polarized in the x direction.

When the input power is increased from zero, first a homogeneous state of zero magnetization is found. In this case there is no y component of the light field. When a threshold pump rate of $P_0 = 1.25 \times 10^5 \text{ s}^{-1}$ is exceeded, a central slightly distorted ring system is found in the orientation, see Fig. 6(k). In the y component of the backward laser beam a central bright spot is found, which is surrounded by ring fragments lying opposite to each other, see Fig. 6(a). After a slight increase of the input pump rate, the patterns found in the orientation and the near field stay nearly the same but occupy a slightly larger area on the Gaussian beam, see Figs. 6(b) and 6(l). The corresponding far field image shows a slightly perturbed ring of high intensity [Fig. 6(g)] demonstrating the emergence of a characteristic wave number.

For an input pump rate of $P_0 = 1.50 \times 10^5 \text{ s}^{-1}$, a pattern of alternating maxima and minima is found in the orientation, see, Fig. 6(m). In the y component of the backward laser beam, shown in Fig. 6(c), a pattern of intensity maxima is found. A ring-like structure of eight intensity maxima is formed slightly off center on the laser beam. The far field

image shows eight peaks at equal wave numbers, the wave vectors of which form vertex angles of $45^\circ \pm 1^\circ$.

At an input pump rate of $P_0 = 1.60 \times 10^5 \text{ s}^{-1}$, a second ring of eight intensity maxima is visible in the image of the y component of the backward laser beam. In the image of the orientation, a corresponding set of eight alternating minima and maxima is found. The far field image shows a set of eight intense maxima with vertex angles of $45^\circ \pm 1^\circ$.

A further increase of the input pump rate results in a further increase of the transverse extent of the near field pattern. In the center of the laser beam a number of circles can be seen, each of them consisting of eight intensity maxima [see Fig. 6(e)]. The far field image is composed of a ring of eight principal modes with at least three clearly visible sets of harmonics. In the corresponding image of the orientation [Fig. 6(o)] a complex pattern can be seen, which also contains characteristic substructures. These substructures are composed of maxima surrounded by eight minima each and minima surrounded by eight maxima. The average value of the orientation remains approximately zero throughout the scan of the input pump rates.

Figure 7 shows the result of three independent runs of the numerical simulation for parameters identical to those of Figs. 6(e), 6(j), and 6(o) with different random initial conditions. The near field images of the linear polarization component orthogonal to the input polarization show different patterns of bright spots. The patterns resemble each other in

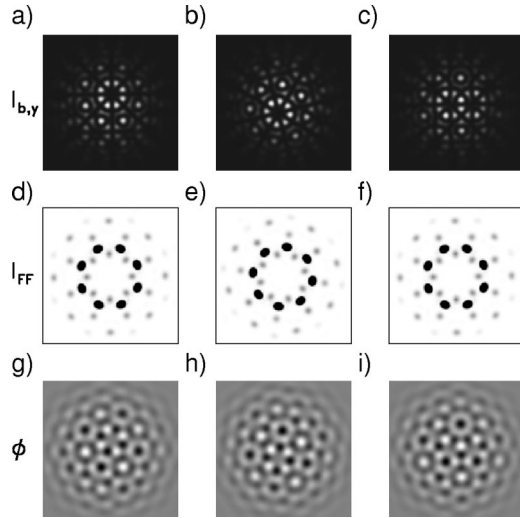


FIG. 7. Eightfold quasipatterns obtained from numerical simulation assuming a Gaussian input laser beam and Dirichlet boundary conditions for the medium. The input laser beam is linearly polarized in the x direction. The images show the result of three runs of the simulation for identical parameters, but different random initial conditions. (a)–(c) Backward near field intensity distribution of the linear polarization component orthogonal to the input polarization. (d)–(f) Total far field intensity distribution. (g)–(i) Transverse distribution of the longitudinally averaged orientation ϕ . Parameters as in Figs. 6(e), 6(j), and 6(o).

the sense that in each of the images a number of rings of eight intensity maxima can be found. A similar observation applies to the patterns present in the orientation of the vapor [Fig. 7(g), 7(h), 7(i)]. Independent of the near field structure, all far field images [Fig. 7(d), 7(e), and 7(f)] show a structure of eight principal modes on a circle, which are separated by angles of $45^\circ \pm 1^\circ$ and at least three other sets of modes, which can be interpreted as the spatial harmonics of the principal modes. These features match the observations in the experiment. The near field images can be interpreted as a cut from a spatially extended quasipattern at different locations.

In order to provide further support for this interpretation, we performed numerical simulations assuming a plane wave input light field with both periodic and Dirichlet boundary conditions for the medium. No qualitative difference could be found between the far field images obtained from the simulations with periodic and those with Dirichlet boundary conditions or between different runs of the simulation. Moreover, the near field patterns show a strong similarity to the patterns obtained in the center of a Gaussian input laser beam. Thus we conclude that the quasipatterns observed in the Gaussian beam would also be selected in a homogeneous system.

Some boundary effects are present close to threshold, though. In numerical simulations with a plane wave input laser beam, the quasipatterns emerge directly at the threshold of the instability. When a Gaussian input laser beam is used, the bifurcation to eightfold quasipatterns goes through an intermediate state in which, as in the experiment, patterns of ring fragments or slightly distorted rings are found. Thus these intermediate patterns are due to finite size effects.

We remark that rhombic two-mode patterns were neither found in numerical simulations with a plane wave input nor with a Gaussian beam. Three-mode patterns occur sometimes during the transient of pattern evolution close to threshold with a plane wave input and periodic boundary conditions, especially if the resolution of the grid in Fourier space is low. With a higher resolution in Fourier space patterns are obtained which are eightfold quasipatterns with a high precision; an ideal quasipattern cannot exist on a grid with periodic boundary conditions.

C. Linear and nonlinear stability analysis

In the following, we will present the result of analytical investigations of the pattern selection process. The way of doing these calculations closely follows the one discussed in Refs. [10,25]. However, we consider the general case of both non-negligible absorption and diffusion. We assume a linearly polarized plane wave input light field. The stress parameter of the system is the sum pump rate of the input light field at the input face of the medium, which is given by $P_{S,0} = \Psi[|\mathcal{E}_{+,f}(\vec{r}_\perp, 0, t)|^2 + |\mathcal{E}_{-,f}(\vec{r}_\perp, 0, t)|^2]$.

Equation (3) possesses a unique stationary, spatially homogeneous solution, which is given by

$$\phi_h \equiv 0, \quad (10)$$

independently of the value of $P_{S,0}$.

Let us now consider a small perturbation $\delta\phi$ of this homogeneous solution. Substituting $\phi = \phi_h + \delta\phi$ yields an equation of motion for the perturbation

$$\begin{aligned} \frac{\partial}{\partial t} \delta\phi = & -(\gamma - D\Delta_\perp) \delta\phi + \frac{1}{2} P_{S,0} (1 - e^{-2\alpha_0 L(1 - \delta\phi)}) \\ & \times (1 + R |\mathbf{P} e^{i\alpha_0 L(\bar{\Delta} + i)(1 + \delta\phi)}|^2) \\ & - \frac{1}{2} P_{S,0} (1 - e^{-2\alpha_0 L(1 + \delta\phi)}) \\ & \times (1 + R |\mathbf{P} e^{i\alpha_0 L(\bar{\Delta} + i)(1 - \delta\phi)}|^2). \end{aligned} \quad (11)$$

As a first step, we will determine the instability threshold and the critical wave number by means of a linear stability analysis. Linearizing Eq. (11) in $\delta\phi$ yields

$$\frac{\partial}{\partial t} \delta\phi = -(\gamma - D\Delta_\perp) \delta\phi - P_{S,0} F (1 + R F) \delta\phi \quad (12)$$

$$- P_{S,0} F R (1 - F) \quad (13)$$

$$\times \left[\cos\left(\frac{d\Delta_\perp}{k_0}\right) - \bar{\Delta} \sin\left(\frac{d\Delta_\perp}{k_0}\right) \right] \delta\phi. \quad (14)$$

with

$$F = e^{-2\alpha_0 L}. \quad (15)$$

Setting

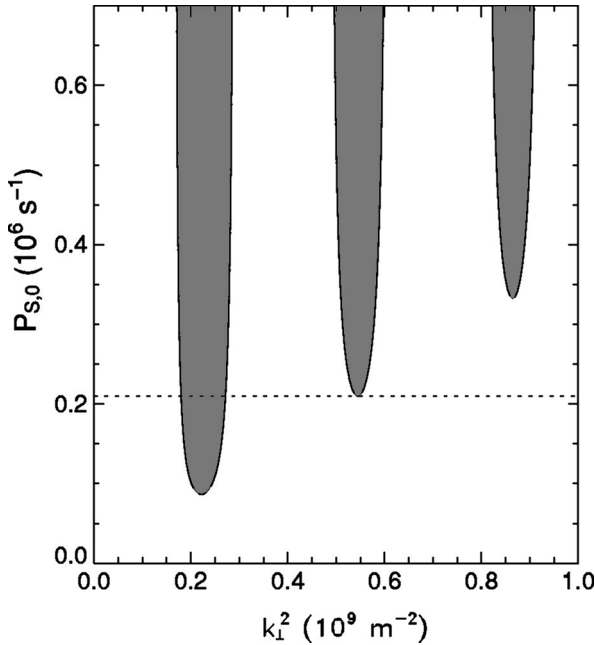


FIG. 8. Result of a linear stability analysis. In the gray shaded regions in the k_{\perp}^2 - $P_{S,0}$ space, the spatially homogeneous solution is unstable vs spatially periodic perturbations. Parameters as in Fig. 6. The dashed horizontal line denotes the maximal pump rate used in the simulations.

$$\delta\phi \sim e^{\mu t + i\vec{k}_{\perp} \vec{r}} + \text{c.c.} \quad (16)$$

yields a growth exponent of the perturbation of

$$\mu = -(\gamma + Dk_{\perp}^2) - P_{S,0}F(1 + RF) \quad (17)$$

$$- P_{S,0}R F(1 - F) \left[\cos\left(\frac{dk_{\perp}^2}{k_0}\right) + \bar{\Delta} \sin\left(\frac{dk_{\perp}^2}{k_0}\right) \right]. \quad (18)$$

μ is a real function of the parameters and k_{\perp}^2 . That means that stationary patterns rather than oscillatory ones are predicted. Figure 8 shows the sign of μ versus $P_{S,0}$ and k_{\perp}^2 . In the gray shaded regions μ is positive and hence the system is unstable with respect to a perturbation at the respective wave number. As for any single feedback mirror system, there is a sequence of instability balloons [36]. Diffusion is rather strong in the present system and hence the minima of the individual instability balloons are shifted to significantly higher pump rates with increasing k_{\perp}^2 . Close to the bifurcation point, the homogeneous state becomes unstable with respect to perturbations of a single wave number given by the minimum of the first instability balloon.

As noted earlier [10,23,25], Eq. (11) possesses an inversion symmetry, i.e., it is invariant under a transformation $\phi \rightarrow -\phi$. As a consequence, any amplitude equation derived from this equation of motion must not include terms of even order in the amplitudes. We derived the amplitude equations by means of a multiple scales approach, similar to the one discussed in Refs. [10,25]. Indeed, the result is a set of coupled amplitude equations of the form

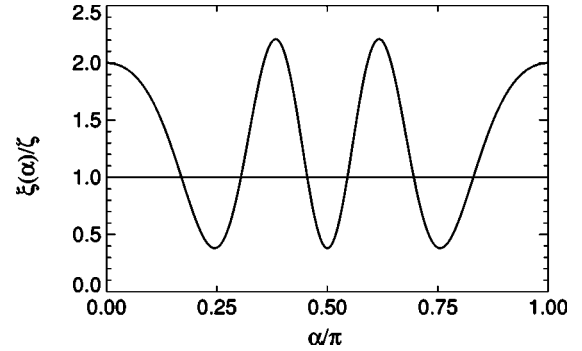


FIG. 9. Result of a multiple scales analysis. Cubic cross coupling coefficient $\xi(\alpha)$ normalized to the cubic self coupling coefficient ζ vs the angle α between the interacting modes. Parameters: $N_{\text{Na}} = 1.4 \times 10^{19} \text{ m}^{-3}$, $\bar{\Delta} = 4.8$, $d = 210 \text{ mm}$, $D = 2.26 \times 10^{-4} \text{ m}^2/\text{s}$, and $\Gamma_2 = 1.04 \times 10^9 \text{ s}^{-1}$.

$$\partial_t A_i = \mu A_i - \zeta A_i |A_i|^2 - A_i \sum_j \xi_{i,j} |A_j|^2 + O(A^5). \quad (19)$$

The functional form of the coefficients is rather complicated; it is given in the appendix. The cubic cross coupling coefficients $\xi_{i,j}$ depend not explicitly on the indices i, j but only on the angle $\alpha_{i,j}$ between the wave vectors of the Fourier modes i and j . It is well known that it is this angular dependence that governs the pattern selection process [8,9].

The amplitude equations (19) are variational; i.e., they can be derived from a Lyapunov function [8–10,25]:

$$\frac{\partial A_i}{\partial t} = - \frac{\partial \mathcal{G}}{\partial A_i^*} \quad \text{with} \quad \frac{\partial \mathcal{G}}{\partial t} \leq 0, \quad (20)$$

which is given by

$$\mathcal{G} = -\mu \sum_{i=1}^N |A_i|^2 + \frac{\zeta}{2} \sum_{i=1}^N |A_i|^4 + \frac{1}{2} \sum_{i=1}^N \sum_{\substack{j=1 \\ j \neq i}}^N \xi(\alpha_{i,j}) |A_j|^2 |A_i|^2. \quad (21)$$

The pattern which minimizes the Lyapunov function is the one expected to emerge most likely at threshold [8–10,25].

The linear stability analysis fixes only the critical wave number k_c at threshold. Due to rotational symmetry, in principle an infinite number of modes with $|\mathbf{k}_{\perp}| = k_c$ might emerge at threshold. However, usually the pattern selected by the nonlinearities is build from a small subset of these modes, the simplest examples being stripes ($N=1$), squares ($N=2$, $\alpha = \pi/2$) or rhombs ($N=2$, $\alpha \neq \pi/2$). For these simple structures the calculation of the values of the Lyapunov function is straightforward. The result is

$$\mathcal{G}_1 = - \frac{\mu^2}{2\zeta} \quad (22)$$

for the stripe patterns and

$$\mathcal{G}_2 = -\frac{\mu^2}{\zeta + \xi(\alpha)} \quad (23)$$

for the two-mode patterns.

Figure 9 shows the angular dependence of the cross-coupling coefficient $\xi(\alpha)$ versus the vertex angle α of the wave vectors of the two Fourier modes for the parameters of Fig. 6. For reasons of simplicity, $\xi(\alpha)$ is normalized to the self-coupling coefficient ζ . Both $\xi(\alpha)$ and ζ are positive. $\xi(\alpha)$ possesses three minima in the interval $[0, \pi]$, one at exactly $\alpha = \pi/2$, one at $\alpha \approx 0.244\pi$, and one at $\alpha \approx 0.756\pi$. The values of ξ in these minima are identical. The qualitative shape of the curve is typical for the present system. The precise location of the minima depends on the experimental parameters, especially on the detuning $\bar{\Delta}$.

For the two-mode problem, this structure of $\xi(\alpha)$ implies that the value of the Lyapunov function is identical for squares ($\alpha = 0.5\pi$) and rhombic two-mode patterns with a vertex angle of $\alpha \approx 0.244\pi$ [8,9,26]. [This degeneracy is lifted in the fifth order of the perturbation expansion [26].] Since the minimum value of $\xi(\alpha)/\zeta$ is smaller than unity, the value of the Lyapunov function for the two-mode patterns is also smaller than the value of the Lyapunov function for stripe patterns [8,9].

When more than two modes are considered, regular solutions of N Fourier modes of equal strength, which are separated by an angle of π/N are an important class of fixed solutions of the amplitude [8–10]. An evaluation of the Lyapunov function for this class of patterns shows that the regular solution with $N=4$ —i.e., a quasipattern with an eightfold rotational symmetry—minimizes the Lyapunov function with respect to any other regular solution. Moreover, since the square pattern minimizes the Lyapunov function of the two-mode problem, the quasipattern with $N=4$ also minimizes the Lyapunov function with respect to any other two-mode solution and to stripes.

The transient occurrence of rhombic patterns in the experiment cannot be explained by these theoretical investigations. For the parameters of Fig. 4, the Lyapunov approach predicts eightfold quasipatterns at instability onset. However, a minimum of the cubic cross-coupling coefficient occurs at $\alpha = 42$ degrees, which agrees reasonably well with the experimentally found vertex angles of the rhombic patterns.

D. Theoretical results: Bifurcation diagram

The results of the theoretical analysis presented in this section are summarized in Fig. 10. The parameters correspond to those of Fig. 5. Figure 10(a) shows a plot of the power threshold of the instability for a Gaussian input laser beam, which is taken as the point where the peak intensity passes the threshold calculated by means of the linear stability analysis for a plane wave input beam. The shape of this threshold curve is similar to the one obtained in the experiment shown in Fig. 5. There is a flat minimum of about 85 mW at a normalized detuning of $\bar{\Delta} = 5.1$, which corresponds to a detuning of $\Delta = 8$ GHz. For values of the normalized

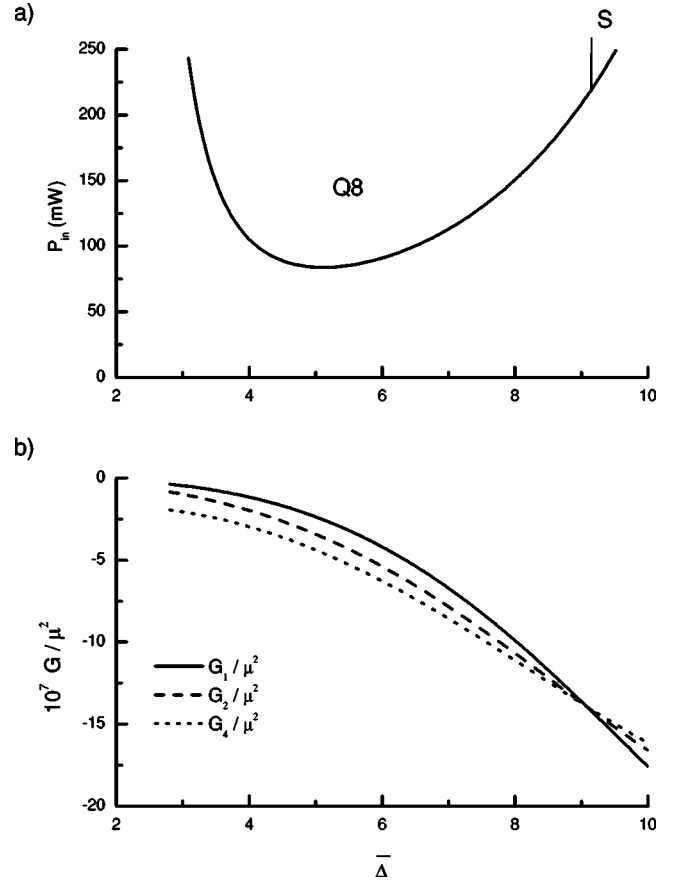


FIG. 10. Bifurcation diagram in dependence on the normalized detuning $\bar{\Delta}$. (a) Threshold curve and predicted patterns at threshold (Q8=quasipatterns, S=stripes). (b) Values of Lyapunov function $\mathcal{G}(N)$ normalized to μ^2 . The numerical parameters are as in Fig. 9 and correspond to the experimental ones of Fig. 5. The power of the input laser beam is calculated using that $P_{in} = c\epsilon_0/(\pi w_0^2) \times (|\mathcal{E}_{+,f}(0)|^2 + |\mathcal{E}_{-,f}(0)|^2)$ and Eqs. (4), (8).

detuning smaller than $\bar{\Delta} = 3.0$ ($\Delta = 5$ GHz) and larger than $\bar{\Delta} = 9.5$ ($\Delta = 15$ GHz) the threshold power exceeds 250 mW, which was the maximum available input power in the experiment (see, e.g., Fig. 5). These values are in reasonable agreement with the experiment findings.

Figure 10(b) shows a plot of the values of the Lyapunov function normalized to the square of the linear growth rate μ^2 for an eightfold quasipattern (\mathcal{G}_4), a two-mode pattern (\mathcal{G}_2) and a stripe pattern (\mathcal{G}_1). The values of the Lyapunov function for any other regular pattern are larger. In a range of the normalized detuning from $\bar{\Delta} = 3.0$ to $\bar{\Delta} = 9.0$ [denoted by Q8 in Fig. 10(a)] the eightfold quasipattern minimizes the Lyapunov functional. For $\bar{\Delta} > 9.0$, the stripe pattern minimizes the Lyapunov functional (region S).

The prediction of eightfold quasipatterns at instability onset in a wide range of the detuning is in qualitative accordance with the experimental findings discussed in Sec. II C. The stripe patterns predicted for large detunings were not observed in the experiment. However, the region in which stripe patterns are predicted at instability onset lies on the

border of the range of parameters which is accessible in the experiment due to power constraints.

IV. DISCUSSION

For positive detuning eightfold quasipatterns are the dominant structures in the experimental system. Since the introduction of the quarter-wave plate in the feedback loop—as discussed in Refs. [25,28] and mentioned in the introduction—is in many respects equivalent to a change of detuning our experimental results are in qualitative agreement to the analysis of Leduc *et al.* [26,27]. This group predicted analytically the occurrence of quasipatterns for negative detuning (and isotropic feedback) in a purely dispersive model and confirmed by some numerical studies that small amounts of absorption do not change the pattern selection.

Leduc *et al.* [26,27] predict in addition square and stripe patterns for the parameters under study. These were not observed in the experiment but this is explained by our theoretical treatment which takes into account the action of the quarter-wave plate in conjunction with absorption and pump depletion. The transition to stripes (and possibly to squares) is shown to occur outside or at the boundary of the range of parameters accessible in the present experiment. We remark that the applicability of the plane wave theory to the analysis of pattern formation in a beam with a Gaussian profile cannot be anticipated beforehand, but needs to be checked for each specific situation. In the system analyzed here, it turns out that the pattern selected with a Gaussian pump and with a plane wave pump is the same as soon as there is a sufficiently large area of the beam above threshold. For this coincidence, it might be helpful that the homogeneous solution is identical to zero for all pump powers and that the instability regions do not have an upper limit (Fig. 8). In contrast, we had found pronounced effects of the beam profile on pattern formation for situations, in which the homogeneous solution changes strongly with pump power and/or in which the instability regions are bounded [e.g., Ref. [37]].

Furthermore, Leduc *et al.* predict a secondary bifurcation from eightfold quasipatterns first to a quasiperiodic three-mode patterns and then to rhombic two-mode patterns far above the instability threshold. This bifurcation could neither be reproduced in the experiment nor in numerical simulations of our model. In both cases, once an eightfold quasipattern was formed it persisted for increasing input pump rate or input power, respectively. The stabilization mechanism for the rhombic patterns proposed by Leduc *et al.* relies on the simultaneous instability of Fourier modes belonging to different instability balloons (multicriticality). Diffusion, which is neglected in the analytical treatment by Leduc *et al.*, shifts the higher instability balloons towards higher pump rates, see Sec. III C, Eq. (18), and Fig. 8. As a consequence, due to the limited input power, true multicriticality is difficult to create in the experiment. Nevertheless, the patterns observed to coexist with eightfold quasipatterns on the wings of the threshold curve in the parameter space spanned by the input power and the detuning (mix in Fig. 5) have a phenomenological similarity with the patterns displayed in Figs. 2, 3 of Ref. [27], though the vertex angle is about 41°

instead of the predicted 48° . To some extent they can be understood to be favorable since the vertex angle of about 41° degrees corresponds roughly to the minima of the cubic-cross coupling coefficient obtained from our model. However, these two and three mode patterns could not be found in numerical simulations starting from noisy initial conditions. Therefore, the exact interpretation of these patterns is still open. They might represent a kind of metastable state which is excited in the experiment due to spatially correlated noise.

Furthermore, one should be aware of the fact that the model—though already quite elaborate and successful—is not complete, e.g., diffraction and refraction within the medium is neglected. This is a common approximation in the description of these kind of systems [10,19,21,23,30] since a full three-dimensional treatment of the propagation of two counterpropagating beams in an extended nonlinear medium is extremely demanding [38], especially if an additional spatial coupling such as diffusion has to be taken into account. The common argument is that the approximation of a thin medium is valid, if the free space propagation length is considerably larger than the length of the medium and indeed we found that this approximation often works very well already for $L \approx 15 \text{ mm} < d \lesssim 75 \text{ mm}$ [e.g., Refs. [7,22,30]]. However, nearly all of these investigations were done in a situation in which the medium behaved self-focusing, i.e., the refractive index increased with increasing intensity. Under these conditions the light tends to be attracted to regions of high intensity [see, e.g., Refs. [39,40]]. Hence a bright spot (e.g., a constituent of a pattern) will stay localized during propagation. In a self-defocusing situation light will be pushed out of the region of high intensity, i.e., modulations tend to be smoothed out. Therefore, one can expect that the threshold for pattern formation will rise. If there are no special configurations of external fields [as in Ref. [30]] self-focusing occurs for positive detuning from the resonance in atomic vapors [e.g., Refs. [41,42]], self-defocusing for a negative one [e.g., Ref. [43]]. This might explain why the quasipatterns were not observed without a quarter-wave plate, where they should form for negative detuning [10], but after the transfer of the instability to positive detuning by the quarter-wave plate. Note however, that even in a thin medium a complete equivalence between the introduction of the quarter-wave plate and a change of detuning [25] holds only in the dispersive limit [28].

As discussed in Sec. III the equations of motion obey an exact inversion symmetry in the case of linear input polarization considered here. Hence quadratic coupling does not have to be considered in the calculation of the cubic cross-coupling coefficient and the system is an example for the stabilization mechanism proposed in Refs. [9,17]. This is also demonstrated by the fact that the cross-coupling function (Fig. 9) displays the characteristic minima in the angle dependence which were postulated in Refs. [9,17] to enforce the selection of the rotational symmetry.

We remark that the apparent existence of quadratic harmonics in Figs. 3 and 7 is due to the fact that we do not observe the dynamical variable (orientation w , respectively ϕ) itself but the transmitted intensity distribution. Even har-

monics are introduced in each of the polarization components by the exponential dependence of the transmitted field on the orientation [Eq. (5)] and the fact that one has to take the modulus squared of the optical field in order to calculate the pump rate [Eq. (6)]. It turns out that the spatial phase between the even harmonics in the pump field is the same for both polarization components so that they cancel out exactly in the driving term for the orientation, since the polarization components pump antagonistically. This ensures the inversion symmetry of the equation of motion (11). Nevertheless, the even harmonics present in the field distribution in the feedback arm might influence the pattern selection since they mix with fundamental wave vectors if one calculates the pump rate. This creates additional driving terms for the fundamentals. Experimentally the influence of the even harmonics in the field distribution on pattern selection can be demonstrated by introducing a Fourier filter in the feedback loop in the manner described in Refs. [44,45]. It turns out that the quasipatterns give way to squares if their harmonics at $2 \cos(\pi/8) \approx 1.848$ times the wave number of the fundamental wave vector are cutoff. These issues will be investigated in more detail in the future.

Finally we discuss the relationship of our results to the observations in the Faraday instability. Eightfold and tenfold quasipatterns were observed [3,6] and received an explanation by amplitude equations derived from the Navier-Stokes equation [12,13]. These amplitude equations are also inversion symmetric and the pattern selection is governed by the cubic cross-coupling coefficient. However, contrary to the case discussed here, the cross-coupling coefficient shows a rather broad minimum around $\pi/2$ in dependence of the angle. This situation is also known to favor quasipattern [8,9,12,13,46], but the order of the quasipattern depends very critically on the shape of the minimum: In Ref. [13] a transition from an eightfold to a fourteenfold via tenfold and twelvefold patterns is predicted for only very small changes of a bifurcation parameter. On the contrary, the rotational order of the pattern is obviously quite fixed, if one has an oscillatory dependence of the cross coupling such as the one depicted in Fig. 9. As discussed in Ref. [10] the existence of this pronounced oscillatory dependence is related to the fact that the Laplace operator is contained up to very high orders in the model equations [cf. Eq. (9)]. Thus such a dependence appears in a natural way in optical systems.

V. SUMMARY

In summary, the observations in the present experimental system qualitatively confirm the core of the theoretical predictions of Leduc *et al.* [10] (concerning the emergence of eightfold quasipatterns) and Scroggie and Firth [25] (concerning the influence of a quarter-wave plate in the feedback loop). However, a direct comparison between the experiment and these predictions is not satisfying. An extended microscopic model accounting for absorption and pump depletion significantly improves the correspondence between experiment and theory. The selection of the eightfold symmetry is consistent with a multiple scale analysis of the microscopic

model. The quasipatterns are stabilized by an oscillatory dependence of the cubic cross-coupling terms on the angle between the interacting wave vectors. This mechanism was postulated in previous theoretical papers [9,17].

ACKNOWLEDGMENTS

This work was supported by the Deutsche Forschungsgemeinschaft.

APPENDIX: DERIVATION OF COEFFICIENTS OF AMPLITUDE EQUATIONS

In the following, the coefficients of the amplitude equations of the two-mode problem will be derived by a multiple scales analysis. The calculations follow the ansatz described in [10,25]. Further details can be found in Ref. [29]. The starting point is the expansion

$$\delta\phi = \epsilon \delta\phi_1 + \epsilon^2 \delta\phi_2 + \epsilon^3 \delta\phi_3 + \dots, \quad (\text{A1})$$

$$P = P_{S,0} + \epsilon p_1 + \epsilon^2 p_2 + \dots, \quad (\text{A2})$$

$$\partial_t = \partial_{T_0} + \epsilon \partial_{T_1} + \epsilon^2 \partial_{T_2} + \epsilon^3 \partial_{T_3} + \dots, \quad (\text{A3})$$

where ϵ is a small parameter. Substitution of this ansatz into Eq. (3) yields a problem of the form

$$\begin{aligned} & [\mathcal{L}_0 + \epsilon \mathcal{L}_1 + \epsilon^2 \mathcal{L}_2](\epsilon \delta\phi_1 + \epsilon^2 \delta\phi_2 + \epsilon^3 \delta\phi_3) \\ & = \epsilon^3 \mathcal{N}_3(\Delta_\perp, \delta\phi_1, \delta\phi_2) + O(\epsilon^4), \end{aligned} \quad (\text{A4})$$

with

$$\begin{aligned} \mathcal{L}_0 = & -\partial_{T_0} - (P_{S,0}F(1+RF) + \gamma - D\Delta_\perp) - P_{S,0}FR(1-F) \\ & \times \left[\cos\left(-\frac{d\Delta_\perp}{k_0}\right) + \bar{\Delta} \sin\left(-\frac{d\Delta_\perp}{k_0}\right) \right], \end{aligned} \quad (\text{A5})$$

$$\begin{aligned} \mathcal{L}_1 = & -\partial_{T_1} - p_1F(1+RF) - p_1FR(1-F) \\ & \times \left[\cos\left(-\frac{d\Delta_\perp}{k_0}\right) + \bar{\Delta} \sin\left(-\frac{d\Delta_\perp}{k_0}\right) \right], \end{aligned} \quad (\text{A6})$$

$$\begin{aligned} \mathcal{L}_2 = & -\partial_{T_2} - p_2F(1+RF) - p_2FR(1-F) \\ & \times \left[\cos\left(-\frac{d\Delta_\perp}{k_0}\right) + \bar{\Delta} \sin\left(-\frac{d\Delta_\perp}{k_0}\right) \right], \end{aligned} \quad (\text{A7})$$

and \mathcal{N}_3 a third order polynomial in $\delta\phi_1$, $\delta\phi_2$ and their spatial derivatives. As a consequence of the inversion symmetry of the microscopic equations, \mathcal{N}_3 does not contain any second order terms in $\delta\phi$ and its spatial derivatives. After calculating the coefficients and undoing the transformations (A1)–(A3), the final result are the coefficients

$$\mu \approx (P_{S,0} - P_c) \mu_p, \quad (\text{A8})$$

$$\zeta = \zeta_3, \quad (\text{A9})$$

$$\xi(\alpha) = \xi_3(\alpha). \quad (\text{A10})$$

The expressions for the coefficients are given by

$$\mu_p = F \left\{ -1 - F R + (-1 + F) R \left[\cos\left(\frac{d k_c^2}{k_0}\right) + \bar{\Delta} \sin\left(\frac{d k_c^2}{k_0}\right) \right] \right\}, \quad (\text{A11})$$

$$\begin{aligned} \zeta_3 = & \{ \alpha_0^2 F L^2 p_0 [2 + (7 + \bar{\Delta}^2) F R] \} + \frac{\alpha_0^2}{2} [3 + \bar{\Delta}^2 (-1 + F) - 15 F] F L^2 p_0 R \cos\left(\frac{d k_c^2}{k_0}\right) \\ & + \frac{\alpha_0^2}{2} \bar{\Delta} [1 + 3 \bar{\Delta}^2 (-1 + F) - 13 F] F L^2 p_0 R \sin\left(\frac{d k_c^2}{k_0}\right) - \frac{\alpha_0^2}{2} (1 + \bar{\Delta}^2) (-1 + F) F L^2 p_0 R \left[\cos\left(\frac{3 d k_c^2}{k_0}\right) + \bar{\Delta} \sin\left(\frac{3 d k_c^2}{k_0}\right) \right] \\ & - \alpha_0^2 F^2 L^2 p_0 R \left[(-1 + \bar{\Delta}^2) \cos\left(\frac{4 d k_c^2}{k_0}\right) - 2 \bar{\Delta} \sin\left(\frac{4 d k_c^2}{k_0}\right) \right], \quad (\text{A12}) \end{aligned}$$

$$\begin{aligned} \xi_3(\alpha) = & 4 \alpha_0^2 F L^2 [1 + (3 + \bar{\Delta}^2) F R] p_0 + 2 \alpha_0^2 [1 + \bar{\Delta}^2 (-1 + F) - 7 F] F L^2 R \left[\cos\left(\frac{d k_c^2}{k_0}\right) + \bar{\Delta} \sin\left(\frac{d k_c^2}{k_0}\right) \right] p_0 \\ & - \alpha_0^2 (1 + \bar{\Delta}^2) (-1 + F) F L^2 R \left[\cos\left(\frac{d k_c^2 [1 - 2 \cos(\alpha)]}{k_0}\right) + \bar{\Delta} \sin\left(\frac{d k_c^2 [1 - 2 \cos(\alpha)]}{k_0}\right) \right] p_0 \\ & - 2 \alpha_0^2 F^2 L^2 R \left[(-1 + \bar{\Delta}^2) \cos\left(\frac{2 d k_c^2 [-1 + \cos(\alpha)]}{k_0}\right) + 2 \bar{\Delta} \sin\left(\frac{2 d k_c^2 [-1 + \cos(\alpha)]}{k_0}\right) \right] p_0 \\ & - 2 \alpha_0^2 F^2 L^2 R \left[(-1 + \bar{\Delta}^2) \cos\left(\frac{2 d k_c^2 [1 + \cos(\alpha)]}{k_0}\right) - 2 \bar{\Delta} \sin\left(\frac{2 d k_c^2 [1 + \cos(\alpha)]}{k_0}\right) \right] p_0 \\ & - \alpha_0^2 (1 + \bar{\Delta}^2) (-1 + F) F L^2 R \left[\cos\left(\frac{d k_c^2 [1 + 2 \cos(\alpha)]}{k_0}\right) + \bar{\Delta} \sin\left(\frac{d k_c^2 [1 + 2 \cos(\alpha)]}{k_0}\right) \right] p_0. \quad (\text{A13}) \end{aligned}$$

These coefficients were evaluated numerically using programs generated automatically by the software package MATHEMATICA.

-
- [1] D. Levine and P.J. Steinhardt, *Phys. Rev. Lett.* **53**, 2477 (1984).
[2] C. Janot, *Europhys. News* **27**, 60 (1996).
[3] B. Christiansen, P. Alström, and M.T. Levinsen, *Phys. Rev. Lett.* **68**, 2157 (1992).
[4] W.S. Edwards and S. Fauve, *Phys. Rev. E* **47**, R788 (1993).
[5] E. Pampaloni, P.L. Ramazza, S. Residori, and F.T. Arecchi, *Phys. Rev. Lett.* **74**, 258 (1995).
[6] D. Binks and W. van de Water, *Phys. Rev. Lett.* **78**, 4043 (1997).
[7] R. Herrero, E. Große Westhoff, A. Aumann, T. Ackemann, Y.A. Logvin, and W. Lange, *Phys. Rev. Lett.* **82**, 4627 (1999).
[8] B.A. Malomed, A.A. Nepomnyashchii, and M.I. Tribel'skii, *Zh. Eksp. Teor. Fiz.* **96**, 684 (1989) [*Sov. Phys. JETP* **69**, 388 (1989)].
[9] H.W. Müller, *Phys. Rev. E* **49**, 1273 (1994).
[10] D. Leduc, M.L. Berre, E. Ressayre, and A. Tallet, *Phys. Rev. A* **53**, 1072 (1996).
[11] R. Lifshitz and D.M. Petrich, *Phys. Rev. Lett.* **79**, 1261 (1997).
[12] W. Zhang and J. Viñals, *Phys. Rev. E* **53**, R4283 (1996).
[13] W. Zhang and J. Viñals, *J. Fluid Mech.* **336**, 301 (1997).
[14] W.S. Edwards and S. Fauve, *J. Fluid Mech.* **278**, 123 (1994).
[15] M.A. Vorontsov and A.Y. Karpov, *J. Opt. Soc. Am. B* **14**, 34 (1997).
[16] M.C. Cross and P.C. Hohenberg, *Rev. Mod. Phys.* **65**, 851 (1993).
[17] M. Bestehorn, *Strukturbildung durch Selbstorganisation in Flüssigkeiten und in Chemischen Systemen*, Reihe Physik Vol. 48 (Verlag Harri Deutsch, Frankfurt am Main, 1995).
[18] G. Giusfredi, J.F. Valley, R. Pon, G. Khitrova, and H.M. Gibbs, *J. Opt. Soc. Am. B* **5**, 1181 (1988).
[19] G. D'Alessandro and W.J. Firth, *Phys. Rev. Lett.* **66**, 2597 (1991).
[20] T. Ackemann and W. Lange, *Phys. Rev. A* **50**, R4468 (1994).
[21] G. Grynberg, A. Maître, and A. Petrossian, *Phys. Rev. Lett.* **72**, 2379 (1994).
[22] A. Aumann, E. Büthe, Y.A. Logvin, T. Ackemann, and W. Lange, *Phys. Rev. A* **56**, R1709 (1997).
[23] M.L. Berre, D. Leduc, E. Ressayre, A. Tallet, and A. Maître, *Opt. Commun.* **118**, 447 (1995).
[24] A. J. Scroggie, Ph. D. thesis, Glasgow, 1995.
[25] A.J. Scroggie and W.J. Firth, *Phys. Rev. A* **53**, 2752 (1996).
[26] D. Leduc, M.L. Berre, E. Ressayre, and A. Tallet, *Phys. Rev. A* **55**, 2321 (1997).
[27] D. Leduc, M.L. Berre, E. Ressayre, and A. Tallet, *Opt. Commun.* **130**, 181 (1996).
[28] T. Ackemann, A. Aumann, E. Grosse Westhoff, Y.A. Logvin, and W. Lange, *J. Opt. B: Quantum Semiclassical Opt.* **3**, S124 (2001).
[29] A. Aumann, Ph. D. thesis, Westfälische Wilhelms-Universität Münster, 1999.

- [30] W. Lange, Y.A. Logvin, and T. Ackemann, *Physica D* **96**, 230 (1996).
- [31] R. W. Boyd, *Nonlinear Optics* (Academic Press, Boston, 1992).
- [32] W. Lange, T. Ackemann, A. Aumann, E. Büthe, and Y.A. Logvin, *Chaos, Solitons Fractals* **10**, 617 (1999).
- [33] F. Mitschke, R. Deserno, W. Lange, and J. Mlynek, *Phys. Rev. A* **33**, 3219 (1986).
- [34] M. Möller and W. Lange, *Phys. Rev. A* **49**, 4161 (1994).
- [35] A. Aumann, T. Ackemann, E. Grosse Westhoff, and W. Lange, *Int. J. Bifurcation Chaos Appl. Sci. Eng.* **11**, 2789 (2001).
- [36] G. D'Alessandro and W.J. Firth, *Phys. Rev. A* **46**, 537 (1992).
- [37] T. Ackemann, Y. Logvin, A. Heuer, and W. Lange, *Phys. Rev. Lett.* **75**, 3450 (1995).
- [38] O. Sandfuchs, F. Kaiser, and M.R. Belic, *Phys. Rev. A* **64**, 063809 (2001).
- [39] Y.R. Shen, *Prog. Quantum Electron.* **4**, 2 (1975).
- [40] J.H. Marburger, *Prog. Quantum Electron.* **4**, 35 (1975).
- [41] J.E. Bjorkholm and A. Ashkin, *Phys. Rev. Lett.* **32**, 129 (1974).
- [42] D. Suter and T. Blasberg, *Phys. Rev. A* **48**, 4583 (1993).
- [43] T. Ackemann, T. Scholz, C. Vorgerd, J. Nalik, L.M. Hoffer, and G.L. Lippi, *Opt. Commun.* **147**, 411 (1998).
- [44] A.V. Mamaev and M. Saffman, *Phys. Rev. Lett.* **80**, 3499 (1998).
- [45] T. Ackemann, B. Giese, B. Schäpers, and W. Lange, *J. Opt. B: Quantum Semiclassical Opt.* **1**, 70 (1999).
- [46] M. Bestehorn and H. Haken, in *Dissipative Structures in Transport Processes and Combustion*, edited by D. Meinköhn Springer Series in Synergetics Vol. 48 (Springer-Verlag, Berlin, 1990).